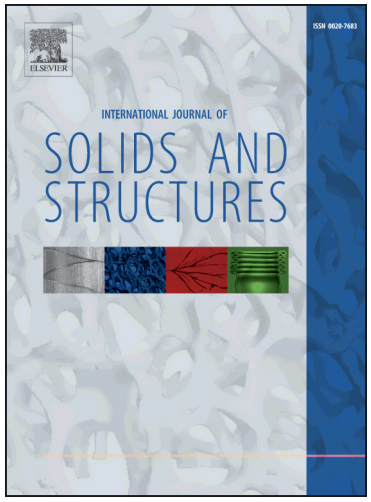

Nonlinear mechanics of non-dilute viscoelastic layered composites

Kashyap Alur, Julien Meaud

PII: S0020-7683(15)00326-1
DOI: http://dx.doi.org/10.1016/j.ijsolstr.2015.07.020
Reference: SAS 8855

To appear in: *International Journal of Solids and Structures*

Received Date: 24 December 2014
Revised Date: 22 June 2015

Please cite this article as: Alur, K., Meaud, J., Nonlinear mechanics of non-dilute viscoelastic layered composites, *International Journal of Solids and Structures* (2015), doi: http://dx.doi.org/10.1016/j.ijsolstr.2015.07.020

Nonlinear mechanics of non-dilute viscoelastic layered composites

Kashyap Alur[a], Julien Meaud[b]

[a]*G. W. Woodruff School of Mechanical Engineering*
Georgia Institute of Technology, Atlanta, GA
[b]*julien.meaud@me.gatech.edu*
G. W. Woodruff School of Mechanical Engineering
Georgia Institute of Technology, Atlanta, GA

Abstract

This paper investigates the nonlinear mechanics of layered composites that include a stiff elastic constituent and a soft viscoelastic constituent. Layered composites buckle with an infinite wavelength at small compressive strains in the case of a high volume fraction of the stiff constituent (the non-dilute case). An iterative algorithm is derived for the finite deformation of viscoelastic non-dilute layered composites with neo-Hookean phases. After validation by comparison to nonlinear finite element simulations, we analyze the effect of initial layer direction, strain rate, and prestrain on the response to time-dependent prescribed compressive strains. Interestingly, these composites have both a very high stiffness prior to buckling and a large energy dissipation capacity in the postbuckling regime. When these composites are subjected to cyclic strains of small amplitude, the effective stiffness and damping properties can be tuned by orders of magnitude by adjusting the prestrain.

Keywords: Layered composites, viscoelasticity, buckling, damping

1. Introduction

Composite materials that consist of parallel plane layers of two different constituents have been a focus of active research in recent years due to the relative simplicity of these microstructures and to the possibility of obtaining multifunctional structures and composites. For example, layered structures that mimic the microstructure of elasmoid fish scales have been designed in order to simultaneously achieve excellent flexibility and protection [6, 31, 35]. The wrinkling of layers due to elastic instability has been proposed as a way to alter elastic wave propagation [33]. Due to axial-shear coupling in layered structures, large rotational motion can be obtained from local compressive loads, which could be used as an actuation mechanism [32]. Layered composites also exist at the nano-scale since the microstructure of block copolymers also consists of parallel layers [22]. Elastic and viscoelastic layered composites are also very common geological structures [4, 25]. Furthermore, investigating the mechanics of layered composites is important as it can be considered as an approximate model for polymers reinforced by elastic fibers, platelets or other similar types of inclusions [21].

Among the possible applications of layered composites, previous work has shown that layered composites with a stiff constituent and a soft viscoelastic constituent can simultaneously achieve high stiffness and high damping [7, 23, 24]. These materials would be very useful in structural applications and in high vibration environments; traditional engineering materials such as metals or polymers do not simultaneously exhibit high stiffness and damping [1, 18]. Viscoelastic layered composites were first analyzed by Chen and Lakes [7] who derived formulae using the linear viscoelastic theory for the

Reuss (loading in the direction normal to the layers) and Voigt (loading in the layer direction) topologies and demonstrated that simultaneously high stiffness and high damping can be achieved with the Reuss topology due to high normal strains in the soft constituent. Meaud and Hulbert subsequently showed that these formulae should take into account Poisson effects, as they are very sensitive to changes in the Poisson's ratio and bulk loss factor of the viscoelastic constituent [23]. Meaud *et al.* [24] later derived the dynamic properties of layered composites when loaded uniaxially in an arbitrary direction. Using optimization studies, they found that the large shear strains in the soft constituent induced by axial shear coupling can be used to simultaneously achieve even higher damping and stiffness than with the Reuss topology [24]. However, the effective properties of viscoelastic layered composites tend to deviate from the linear viscoelastic theory even at small macroscopic strains according to nonlinear finite element simulations [24] .

While elastic instability and buckling have been traditionally considered a failure mechanism for structures and composite materials due to a loss in load-bearing capacity (see for example [5]), harnessing these instabilities to obtain tunable and/or multifunctional structures and materials has been a topic of active research in recent years [2, 30, 17, 33, 39]. The buckling of fibre-reinforced and layered composites has been extensively investigated since the work of Rosen in the 1960s [29] because it is one of the major failure mechanism for these composites. In particular, Triantafyllidis and Maker [38] derived analytical solutions for the bifurcation instabilities of layered composites under compressive loading. Nestorovic and Triantafyllidis [26] extended the analysis to combined normal and shear loading. For fibre reinforced

composites of infinite size, Parnes and Chiskis [28] demonstrated that the wavelength of the instability is infinite in the non-dilute case (*i.e.*, when the volume fraction of the stiff constituent is high) and finite in the dilute case (*i.e.*, when the volume fraction of the stiff constituent is low). Rudykh and deBotton [34] analyzed the buckling of hyperelastic fiber-reinforced composites. In the case of elastic phases (*i.e.*, no viscoelasticity), the finite deformation and postbuckling response of layered composites has been analyzed in [21, 19, 31]. In particular, Lopez-Pamies and Ponte-Castañeda [21] analyzed how the layer direction tends to change upon loading in non-dilute layered composites when certain deformation modes (such as pure shear) are applied. Rudykh and Boyce [31] derived closed form formulae for the finite deformation of hyperelastic layered composites (in the non-dilute case) and showed that rotation of the layers occurs even under purely compressive loads. The formulae derived by Rudykh and Boyce [31] are extended in this paper to the case of viscoelastic layered composites. Li *et al.* [19] investigated the transition from short wavelength wrinkling to longwave instabilities for elastic layered composites using analytical, computational and experimental methods.

The finite deformation mechanics of viscoelastic layered composites has not been extensively investigated. However, Biot [4] analyzed the creep buckling of viscoelastic layered composites under confined conditions. Furthermore, some relevant research has been published regarding the buckling of fibre reinforced viscoelastic composites [3] and of thin films on viscous or viscoelastic substrates [15, 14, 13, 16]. For these composites and structures, multiple buckling modes with finite wavelengths can exist. Most of these pa-

pers are focused on determining the dominant buckling wavelength and the growth rate of the dominant buckling mode under constant stress. The instability of a thin film on a viscous substrate has been extensively analyzed by Huang and Suo in a series of papers [15, 14]. Huang *et al.* [13, 16] investigated the modes of instability and the kinetics of wrinkling for a thin film on a viscoelastic substrate. While the wavelength of the buckling mode can change over time in the case of thin film on viscous or viscoelastic substrates, only an infinite wavelength should be present in the case of a non-dilute layered composites. However, despite the relative simplicity of the mode of deformation, we demonstrate in this paper that interesting nonlinear viscoelastic properties can be obtained with these composites.

The goal of this paper is to explore the nonlinear mechanics of viscoelastic layered composites under finite deformation. The composites consist of two phases: a stiff elastic constituent and a soft viscoelastic constituent. First, an elastic buckling analysis is used to gain insight into the finite deformation mechanics of the viscoelastic composites. We derive an iterative algorithm for the finite deformation response of viscoelastic layered composites in the case of neo-Hookean incompressible phases. After validation of this algorithm by comparison with finite element simulations, we perform a parametric study regarding the effects of varying the strain rate, prestrain, and initial layer direction on the finite deformation mechanics. While the theoretical formulae and algorithm are derived for composites of infinite size with incompressible constituents, we use finite element simulations to demonstrate that compressibility has a negligible effect on the response and to determine the minimum size needed to approximate the theoretical results for infinite size.

2. Theoretical and numerical modeling

In this paper A refers to the stiff elastic material while B refers to the soft viscoelastic material. The stress, strain and effective properties refer to the values obtained for uniaxial loading in the vertical direction, X (see Fig. 1).

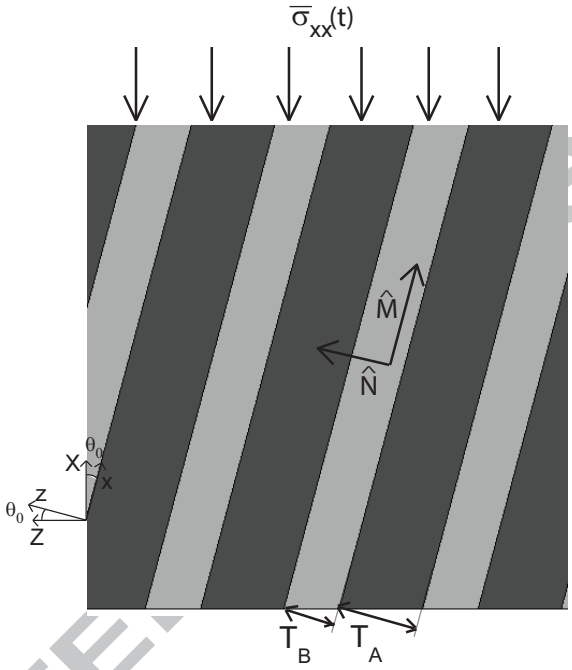

Figure 1: Layered composite with materials A and B. T_A and T_B denote the layer thicknesses. The volume fraction of material A is $\phi_A = T_A/(T_A + T_B)$. The x axis and the unit vector $\hat{M}$ are in the layer direction while the z axis and the unit vector $\hat{N}$ are perpendicular to the layer direction. The composite is loaded in the X direction. θ_0 is angle between the X axis and the layer direction in the undeformed configuration.

2.1. Linear buckling theory for elastic layered composites

While this paper focuses on the nonlinear mechanics of viscoelastic layered composites, we first investigated the buckling of elastic layered composites to determine the transition from dilute (finite buckling wavelength) to non-dilute (infinite buckling wavelength) composites. An infinite wavelength is later used as an assumption in the derivation of the finite deformation response of viscoelastic layered composites. For the buckling analysis, the initial angle, θ_0, is assumed to be 0.

Parnes and Chiskis [28] derived equations for the critical buckling wavelength, L_{cr}, and the critical buckling strain of elastic fibre reinforced composites, ϵ_{cr}. These equations were derived using the plane stress assumption; the stiff fibres were modeled as Euler Bernoulli beams. In order to model the buckling of layered composites, we modified the equations and used a plane strain assumption and a thin plate theory for the stiff layers. While two modes (a shear mode and a transverse mode) are known to exist for the buckling of polymers reinforced by elastic fibers and layered composites [29, 28], Parnes and Chiskis showed that the shear mode has a lower critical strain than the transverse mode [28]. Therefore only the shear buckling mode was considered. The expression for the critical strain is the same as given in [28] for the plane stress assumption:

$$\epsilon_S = \Gamma\Big[2 + \frac{1+f_1}{\eta_f}\Psi_S\Big] + \frac{\eta_f^2}{3} \tag{1}$$

where f_1 is given by $f_1 = 1/(1-2\nu_A)$, where ν_A is the Poisson's ratio of phase A, Γ is a function of the material parameters and Ψ_S is given by:

$$\Psi_S = \frac{\Big(\sinh(\eta_m) - \eta_f\cosh(\eta_m)\Big)^2}{(2+f_1)\sinh(\eta_m)\cosh(\eta_m) + f_1\eta_m} \tag{2}$$

η_f and η_m are functions of the thickness of the stiff layer, T_A, thickness of the soft layer, T_B, and wavelength, L:

$$\eta_f = \frac{\pi T_A}{L} \tag{3}$$

$$\eta_m = \frac{\pi T_B}{L} \tag{4}$$

Since we use a plane strain assumption here, the expression for Γ is changed from the expression given in [28] to the following expression:

$$\Gamma = \frac{1-\nu_A^2}{1+\nu_B}\frac{E_B}{E_A} \tag{5}$$

where E_A and E_B are the Young's moduli of materials A and B, respectively; ν_B is the Poisson's ratio of material B. The buckling strain, ϵ_{cr}, and the buckling wavelength, L_{cr}, are found numerically by finding the minimum value of ϵ_S in Eq. 1.

2.2. Finite deformation response of viscoelastic layered composites

Incremental equations were derived for the finite deformation mechanics of viscoelastic composites in the quasi-static regime (*i.e.*, the dimensions are assumed to be small enough such that the effect of inertia can be neglected). These equations are an extension of the equations given by Rudykh and Boyce [31] for hyperelastic layered composites (without viscoelasticity). The composites are assumed to have infinite dimensions and to be non-dilute (such that the buckling wavelength is infinite at any strain rate). Because of these assumptions, the stresses and strains are uniform within each phase. As in [31], we assume here that both phases are incompressible. The macroscopic deformation gradient, $\bar{\mathbf{F}}$, is written as:

$$\bar{\mathbf{F}} = \phi_A \mathbf{F}^{\mathbf{A}} + \phi_B \mathbf{F}^{\mathbf{B}} \tag{6}$$

where $\mathbf{F^A}$ and $\mathbf{F^B}$ are the deformation gradients in phases A and B, respectively; ϕ_A and ϕ_B are the volume fractions of phases A and B, respectively. As described in [31], the displacement continuity condition gives the following equations for $\mathbf{F^A}$ and $\mathbf{F^B}$:

$$\mathbf{F^A} = \bar{\mathbf{F}}(\mathbf{I} + \phi_B \alpha(t) \hat{\mathbf{M}} \otimes \hat{\mathbf{N}}) \tag{7}$$

$$\mathbf{F^B} = \bar{\mathbf{F}}(\mathbf{I} - \phi_A \alpha(t) \hat{\mathbf{M}} \otimes \hat{\mathbf{N}}) \tag{8}$$

where $\mathbf{I}$ is the identity matrix, $\hat{\mathbf{M}}$ is a unit vector in the layer direction and $\hat{\mathbf{N}}$ is the unit normal vector (in the undeformed configuration, see Fig. 1). $\alpha(t)$ is a time-dependent coefficient that is found, as in [31], using the following traction continuity condition at the interface between phase A and B:

$$\boldsymbol{\sigma}^A.\mathbf{n} = \boldsymbol{\sigma}^B.\mathbf{n} \tag{9}$$

where $\mathbf{n}$ is the unit vector normal to the interface in the current configuration; $\boldsymbol{\sigma}^A$ and $\boldsymbol{\sigma}^B$ are the Cauchy stresses in phases A and B, respectively. Material A is modeled as a neo-Hookean hyperelastic material. Material B is modeled using a finite strain viscoelastic theory with internal variables, that was proposed by Holzapfel [11, 12]. Only one viscoelastic branch is included here (see Fig. 2) but the extension to more than one viscoelastic branch would be straightforward. The Cauchy stress in material B is related to the second Piola-Kirchoff stress in material B, $\mathbf{S^B}$, by:

$$\boldsymbol{\sigma}^B = \mathbf{F^B S^B} (\mathbf{F^B})^\mathbf{T} \tag{10}$$

As in [12], the deviatoric part of the 2nd Piola-Kirchoff stress, $\mathbf{S_D^B}$, is written as:

$$\mathbf{S_D^B} = \mathbf{S_\infty^D} + \mathbf{Q}_\alpha \tag{11}$$

where $\mathbf{S}_{\infty}^{\mathbf{D}}$ is the long-term deviatoric part and $\mathbf{Q}_{\alpha}$ is the non-equilibrium part of the second Piola-Kirchoff stress. The long-term elastic behavior is governed by a neo-Hookean strain energy potential with a shear modulus of value $\mu_B^{(\infty)}$, such that:

$$\mathbf{S}_{\infty}^{\mathbf{D}} = \mu_B^{(\infty)}\Big[\mathbf{I} - \frac{Trace(\mathbf{C_B})}{3}\mathbf{C_B}^{-1}\Big] \tag{12}$$

where $\mathbf{C_B}$ is the right Cauchy-Green tensor in phase B. The non-equilibrium stress is governed by the following rate equation:

$$\dot{\mathbf{Q}}_{\alpha} + \frac{\mathbf{Q}_{\alpha}}{\tau_{\alpha}} = \dot{\mathbf{S}}_{\alpha}^{\mathbf{D}} \tag{13}$$

where τ_{α} is the relaxation time constant and $\mathbf{S}_{\alpha}^{\mathbf{D}}$ is assumed (as in [11, 12]) to be given by a neo-Hookean strain energy potential that is proportional to the strain energy for the long-term behavior. With this assumption, $\mathbf{S}_{\alpha}^{\mathbf{D}}$ can be written as:

$$\mathbf{S}_{\alpha}^{\mathbf{D}} = \mu_B^{(\alpha)}\Big[\mathbf{I} - \frac{Trace(\mathbf{C_B})}{3}\mathbf{C_B}^{-1}\Big] \tag{14}$$

where $\mu_B^{(\alpha)}$ is the shear modulus for the non-equilibrium behavior.

We follow the iterative algorithm described by Holzapfel [11, 12] for finite deformation viscoelastic models to increment the stress in material B. At step i of the algorithm, the value of $\mathbf{Q}_{\alpha}\big|_{i+1}$ is computed using the following equation:

$$\mathbf{Q}_{\alpha}\big|_{i+1} = \beta_{\alpha}^{\infty} exp(\xi_{\alpha})\ \mathbf{S}_{\infty}^{D}\big|_{i+1} + \mathbf{H}_{\alpha}\big|_{i} \tag{15}$$

where $\beta_{\alpha}^{\infty} = \mu_B^{(\alpha)}/\mu_B^{(\infty)}$; and $\xi_{\alpha} = -\frac{\Delta t}{2\tau_{\alpha}}$, where τ_{α} is the relaxation time constant and Δt is the time-step; $\mathbf{H}_{\alpha}\big|_{i}$ is a history term (known from the previous time step); and $\mathbf{S}_{\infty}^{\mathbf{D}}\big|_{i+1}$ is calculated using Eq. 12. Before starting

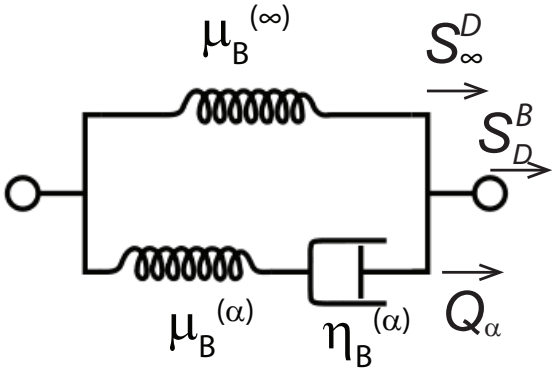

Figure 2: Rheological model for material B. The deviatoric part of the 2nd Piola-Kirchoff stress, $\mathbf{S_D^B}$, is the sum of the long-term 2nd Kirchoff-Piola stress, $\mathbf{S_\infty^D}$ and of the non-equilibrium stress, $\mathbf{Q}_\alpha$. The long-term behavior is modeled using a neo-Hookean strain energy potential with a shear modulus of value $\mu_B^{(\infty)}$. The non-equilibrium behavior is governed by a neo-Hookean potential with a shear modulus of value $\mu_B^{(\alpha)}$. The relaxation time constant, $\tau_B^{(\alpha)}$, given in Table 1, is given by $\tau_B^{(\alpha)} = \eta_B^{(\alpha)}/\mu_B^{(\alpha)}$.

the next iteration of the algorithm, the value of $\mathbf{H}_\alpha|_{i+1}$ is computed using the equation [12]:

$$\mathbf{H}_\alpha|_{i+1} = exp(\xi_\alpha)\Big[exp(\xi_\alpha)\ \mathbf{Q}_\alpha|_{i+1} - \beta_\alpha^\infty\ \mathbf{S}_\infty^D\big|_{i+1}\Big] \tag{16}$$

An equation for the value of $\alpha(t)$ at time step $i+1$, α_{i+1}, is needed, which requires determining the Cauchy stress in phase B. Using Eqs. 11, 15 and 16, the Cauchy stress at step $i+1$ can be written:

$$\boldsymbol{\sigma}^B\big|_{i+1} = -\ p^B\big|_{i+1}\,\mathbf{I} + \Big[1 + \beta_\alpha^\infty exp(\xi_\alpha)\Big]\ \boldsymbol{\sigma}_\infty^D\big|_{i+1} + \mathbf{F_{i+1}^B}\ \mathbf{H}_\alpha|_i\ (\mathbf{F_{i+1}^B})^T \tag{17}$$

where $p^B\big|_{i+1}$ is the hydrostatic pressure at step $i+1$ in material B, $\boldsymbol{\sigma}_\infty^D\big|_{i+1} = \mathbf{F_{i+1}^B}\ \mathbf{S_D^B}\big|_\infty\ (\mathbf{F_{i+1}^B})^\mathbf{T}$. Since the long-term behavior of B is neo-Hookean,

$$\boldsymbol{\sigma}_\infty^D\big|_{i+1} = \mu_\infty^B\Big[\mathbf{b_{i+1}^B} - \frac{1}{3}Trace(\mathbf{b_{i+1}^B})\mathbf{I}\Big] \tag{18}$$

where $\mathbf{b}^B$ denotes the left Cauchy-Green tensor in phase B. Projecting the traction continuity equation onto the vector $\bar{\mathbf{F}}_{\mathbf{i+1}}\hat{\mathbf{M}}$, we obtain equation for the value of α at time step $i+1$:

$$\alpha_{i+1} = \frac{\Big(\Big[1+\beta_\alpha^\infty exp(\xi_\alpha)\Big]\mu_\infty^B - \mu_A\Big)\bar{\mathbf{F}}_{\mathbf{i+1}}\hat{\mathbf{N}}.\bar{\mathbf{F}}_{\mathbf{i+1}}\hat{\mathbf{M}} + a}{\Big(\mu_A\phi_B + \Big[1+\beta_\alpha^\infty exp(\xi_\alpha)\Big]\mu_\infty^B\phi_A\Big)\bar{\mathbf{F}}_{\mathbf{i+1}}\hat{\mathbf{M}}.\bar{\mathbf{F}}_{\mathbf{i+1}}\hat{\mathbf{M}} + b} \tag{19}$$

where

$$a = (\bar{\mathbf{F}}_{\mathbf{i+1}}\ \mathbf{H}_\alpha|_i\,\hat{\mathbf{N}}).(\bar{\mathbf{F}}_{\mathbf{i+1}}\hat{\mathbf{M}}) \tag{20}$$

$$b = \phi_A(\bar{\mathbf{F}}_{\mathbf{i+1}}(\hat{\mathbf{M}}\otimes\hat{\mathbf{N}})\ \mathbf{H}_\alpha|_i\,\hat{\mathbf{N}}).(\bar{\mathbf{F}}_{\mathbf{i+1}}\hat{\mathbf{M}}) \tag{21}$$

Note that if the viscoelasticity of material B is not taken into account, $a = b = 0$, and the value for α_{i+1} matches the expression given in [31] for hyperelastic layered composites.

An incremental algorithm was implemented in order to find the macroscopic stress component $\bar{\sigma}_{XX}$ as a function of time. The algorithm starts with the value $\mathbf{H}_\alpha|_0 = \mathbf{0}$ for phase B. At each iteration i, the value of $\mathbf{H}_\alpha|_\mathbf{i}$ is known. The value of the macroscopic stretch, $\bar{\lambda}_X$, is incremented. The value of the macroscopic shear, $\bar{\gamma}_{i+1}$, is first found by solving the equation $\bar{\sigma}_{XZ}|_{i+1} = 0$. Then the value of $\bar{\sigma}_{XX}|_{i+1}$ is computed. For the finite deformation response of composites with initially vertical layers ($\theta_0 = 0$), the simulations were obtained by assuming that the initial angle has a small finite value ($\theta_0 = 1\times10^{-2}$ deg) in order to take into account the effect of small imperfections. This value was chosen such that (1) the composites buckle at any strain rate and (2) using a lower value would not significantly change the stress vs strain curve.

2.3. Finite element modeling

Numerical simulations were conducted using the nonlinear finite element code ABAQUS [9]. The model was meshed with two-dimensional 4-node bilinear, reduced integration hybrid elements with constant pressure and hourglass control (CPE4RH elements) in order to model incompressible and nearly incompressible materials. Periodic boundary conditions were used in order to model composites of infinite size [23, 27] by applying the following constraint equations to the displacement of nodes on the edges of the unit cell:

$$U_X|_{top} - U_X|_{bottom} - U_X|_{TL} = 0 \tag{22}$$

$$U_Z|_{top} - U_Z|_{bottom} - U_Z|_{TL} = 0 \tag{23}$$

$$U_X|_{left} - U_X|_{right} = 0 \tag{24}$$

$$U_Z|_{left} - U_Z|_{right} - U_Z|_{BR} = 0 \tag{25}$$

$$U_Z|_{TR} - U_Z|_{BR} - U_Z|_{TL} = 0 \tag{26}$$

$$U_X|_{TR} - U_X|_{TL} = 0 \tag{27}$$

where the superscripts *top*, *bottom*, $left$ and *right* refer to interior nodes on the top, bottom, left and right edges of the unit cell, respectively; the superscripts BL, BR, TL and TR refer to bottom left, bottom right, top left and top right nodes of the unit cell, respectively. $U_X|_{TL}$ is a prescribed function of time. In order to constrain rigid body motion, $U_Z|_{BL} = U_X|_{BL} = U_X|_{BR}$=0. Python scripting was used [9] to automate the meshing and simulation process. A representative unit cell is shown in Fig. 3.

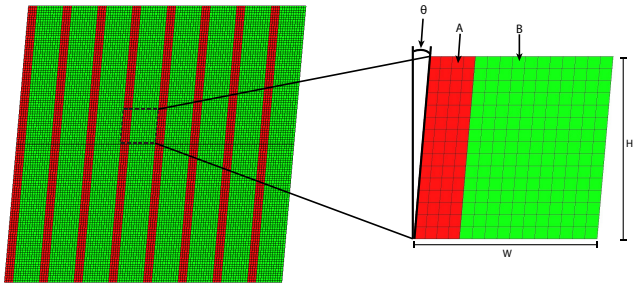

Figure 3: Finite element model in ABAQUS. θ refers to the angle with respect to the vertical direction. Numerical results were obtained using periodic boundary conditions with a unit cell of width, W, and height, H.

2.3.1. Buckling analysis

Finite element simulations were used to validate the theoretical equations that were derived for the critical buckling strain, ϵ_{cr}, and the buckling wavelength, L_{cr}, of elastic layered composites. To obtain these numerical values, the BUCKLE procedure was used in ABAQUS/Standard [9]. If the composite buckles with a finite wavelength, L_{cr}, the buckling shape is a periodic shape of period L_{cr} in the X direction. However, a unit cell of height H with periodic boundary conditions can only deform with a shape of period H/i, where i is any positive integer. Therefore, in order to compute the true value for ϵ_{cr} and L_{cr} using the finite element code, we first computed the theoretical values for the buckling wavelength, $L_{cr}|_{th}$. We then ran the buckling simulations with a unit cell of height $H >> L_{cr}|_{th}$ (typically we chose $H = 20 \times L_{cr}|_{th}$). With this choice, the buckling wavelength predicted by ABAQUS, $L_{cr}|_{FEM}$, was a discrete value that was equal to or directly adjacent to the expected value for $L_{cr}|_{th}$. A more elegant approach would have been to use Bloch wave analysis for a unit cell of height H (where H can

take any value) [8, 2] or the adaptive representative volume element recently proposed by Ton *et al.* [37]. However, since the main goal of these buckling simulations was to validate the buckling theory and to select appropriate volume fractions for non-dilute composites, the approach described above is sufficient. In the case of an infinite buckling wavelength, the height H of the unit cell has no influence on the results. For all simulations, the width of the unit cell was chosen to include only one layer of the phase A and one layer of phase B, since the theory predicts that the shearing mode has a lower critical strain than the transverse mode [28].

2.3.2. Finite deformation simulation

Finite deformation simulations were conducted in ABAQUS/Standard using general Dynamic, Implicit steps while taking into account nonlinear geometrical effects. Most simulations were run for the case of initially vertical layers (corresponding to an initial angle, θ_0, of 0 degree). As in the theoretical results, we used a very small initial angle to mimic the presence of small geometric imperfections and to attain realistic results. Since the first buckling mode is similar to a change in the angle θ, almost identical results would be obtained if small imperfections proportional to the first buckling mode were added instead of using a small non-zero value for θ_0.

2.4. Material models and parameters

Model parameters are listed in Table 1. Two different models were used for material A. The first model corresponds to an incompressible neo-Hookean strain energy potential:

$$\Psi = \frac{\mu_A}{2}(I_1 - 3) \tag{28}$$

where I_1 is the first strain invariant and μ_A is the initial shear modulus of material A. The 2nd model corresponds to a compressible neo-Hookean strain energy potential:

$$\Psi = \frac{\mu_A}{2}(I_1 - 3) + \frac{K_A}{2}(J-1)^2 \tag{29}$$

where J is the Jacobian determinant and K_A is the initial bulk modulus of material A. The properties of material A were chosen such that the plane strain modulus of material A, $\bar{E}_A = (E_A)/(1-\nu^2)$, is similar to the plane strain modulus of steel. Material B was modeled as a standard linear solid using the finite deformation viscoelastic model in ABAQUS. This model is equivalent to the finite deformation viscoelastic model used in the theory (see Appendix C). The deviatoric part of the instantaneous stress was modeled using an incompressible neo-Hookean strain energy potential. The parameters for material B were chosen to resemble those of a high loss polyurethane [36]. The mechanical properties of material B as a function of time and temperature are shown in Fig. 4. In particular, note the strong rate-dependence of the constant strain rate response (Fig. 4B).

Both materials were considered to be incompressible for the results obtained with the theoretical model. Most of the numerical results were obtained with an incompressible model for material A. In the incompressible case, the value of the initial shear modulus of material A, μ_A, was chosen such that the plane strain modulus, $\bar{E}_A$, was equal to its value in the compressible case. Simulations demonstrate that the assumption of incompressibility of material A has limited influence on the numerical results (see Fig. 11).

Table 1: Model parameters for material A and material B

Symbol	Description	Value
μ_A	Initial shear modulus (compressible)	$76,900$ MPa
	Initial shear modulus (incompressible)	54,900 MPa
K_A	Initial bulk modulus (compressible)	$166,700$ MPa
$\mu_B^{(\infty)}$	Long-term shear modulus	1.115 MPa
$\mu_B^{(\alpha)}$	Viscoelastic branch shear modulus	150 MPa
$\tau_B^{(\alpha)}$	Relaxation time constant	0.15 s

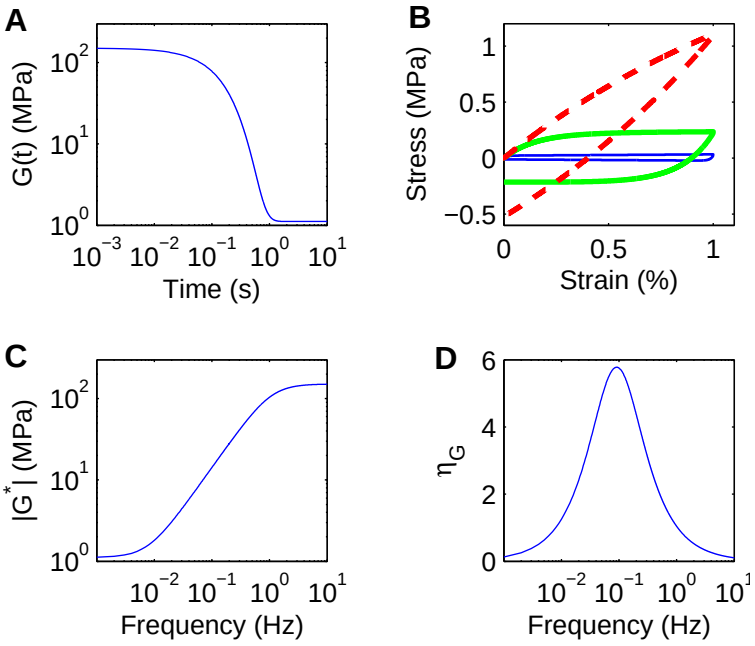

Figure 4: Mechanical properties of material B. A. Relaxation shear modulus vs time. B. Shear stress vs shear strain for loading/unloading at a constant shear strain rate of 0.1, 1 and 10%/s. C. Dynamic shear modulus, $|G^*|$, vs frequency. D. Shear loss factor, η_G, vs frequency

3. Results

3.1. Buckling of elastic layered composites

Both the theory and finite element simulations were first used to determine the critical buckling wavelength and critical buckling strain of elastic layered composites of infinite size. Figs. 5A and B show the nondimensional wavenumber ($\bar{k}_{cr} = Wk_{cr} = (2\pi W)/L_{cr}$, where W is the width of the unit cell and L_{cr} is the critical buckling wavelength) as well as the critical strain, ϵ_{cr}, as functions of the volume fraction of material A, ϕ_A. Since material B is a viscoelastic material, we considered two different values for the Young's modulus of material B: the long-term Young's modulus, $E_B^{(\infty)}$, as well as the instantaneous Young's modulus, $E_B^{(0)} = E_B^{(\infty)} + E_B^{(\alpha)}$. $E_B^{(\infty)}$ and $E_B^{(0)}$ correspond to the lower and upper bounds, respectively, for the time-dependent Young's modulus of material B. The numerical results demonstrate that there is excellent agreement between simulation and theory. Three different cases can be identified in Fig. 5A: (1) when $\phi_A < 1\%$, $k_{cr} \neq 0$ both in the case $E_B = E_B^{(\infty)}$ and $E_B = E_B^{(0)}$; (2) when $1\% < \phi_A < 5\%$, $k_{cr} \neq 0$ if $E_B = E_B^{(0)}$ and $k_{cr} = 0$ if $E_B = E_B^{(\infty)}$; (3) when $\phi_A > 5\%$, $k_{cr} = 0$ both in the case $E_B = E_B^{(\infty)}$ and $E_B = E_B^{(0)}$. The value of ϵ_{cr} decreases monotonically as ϕ_A is increased (Fig. 5B). For any given value of ϕ_A, ϵ_{cr} is higher in the case $E_B = E_B^{(0)}$ than in the case $E_B = E_B^{(\infty)}$, which indicates that increasing E_B tends to increase the buckling strain of the composite. Fig. 5C illustrates the buckling shape in the case $\bar{k}_{cr} = 0$ (which corresponds to $L_{cr} = \infty$) while Fig. 5D is an example of the buckling shape in the case $\bar{k}_{cr} \neq 0$ (which corresponds to $0 < L_{cr} < \infty$).

These numerical results give important qualitative information regarding

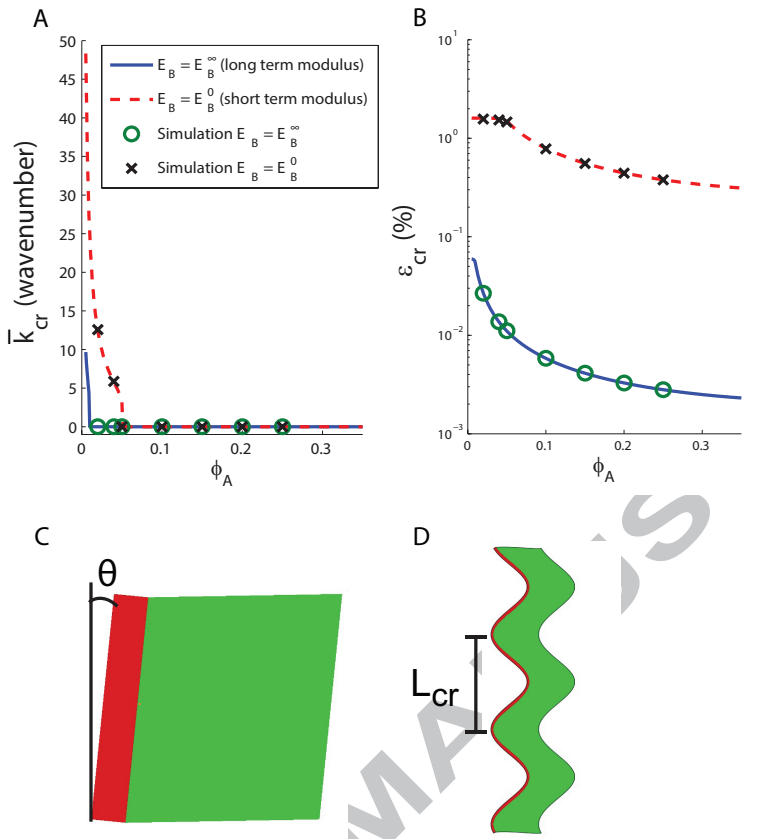

Figure 5: Dependence of the buckling wavenumber and critical strain on the volume fraction on material A and the Young's modulus of material B. A. Non-dimensional wavenumber, $\bar{k}_{cr}$, vs ϕ_A for long and short term E_B. B. Critical strain vs ϕ_A for long and short term E_B. C. Buckling shape with infinite wavelength ($\bar{k}_{cr}$=0) for non-dilute composites. In that case, the layers deform but remain straight. The amplitude of the buckling shape is parameterized by the angle θ. D. Buckling shape with finite wavelength, L_{cr}, for dilute composites.

the finite deformation response of viscoelastic layered composites. The relaxation modulus of a viscoelastic material decreases as a function of time (see Fig. 4A). If the viscoelastic composite is loaded in compression at a constant

strain rate, the composite will buckle with an infinite wavelength provided that $\phi_A > 5\%$. If $1\% < \phi_A < 5\%$, the mode of deformation might progressively change from a small finite wavelength to a larger finite or possibly infinite wavelength (depending on the strain rate). If $\phi_A < 1\%$, the composite will deform with a finite buckling wavelength (that might increase over time). This paper deals with the case of an infinite wavelength (at any strain rate), which corresponds to $\phi_A > 5\%$ with the parameters used here. We refer to this case as the non-dilute case. Since the buckling strain is higher in the case $E_B = E_B^{(0)}$ than in the case $E_B = E_B^{(\infty)}$ (Fig. 5B), the buckling strain is expected to be higher at high strain rates than at low strain rates in the case of a viscoelastic composite.

3.2. Finite deformation for viscoelastic layered composites: constant rate response

The finite deformation response of viscoelastic layered composites subjected to uniaxial compression at a constant strain rate was analyzed in order to characterize the nonlinear mechanics of these composites. The composites are first loaded to a compressive engineering strain of amplitude ϵ_{max} and then unloaded at the same strain rate. Note that in this paper compressive strains and stresses are denoted by positive values. All numerical results are obtained for $\phi_A = 25\%$.

3.2.1. Validation of the finite deformation theory

The finite deformation theory for viscoelastic layered composites was validated by comparison to finite element simulations. The stress vs. strain response was plotted for small and large initial angles (1 and 45 degrees) and

for a broad range of strain rates (0.1 to 10%/s). As shown in Fig. 6, the theory (shown in solid lines) and the simulated response (dotted lines) match exactly. Thus, the finite deformation theory was used with confidence for all the results for infinite size composites with incompressible constituents.

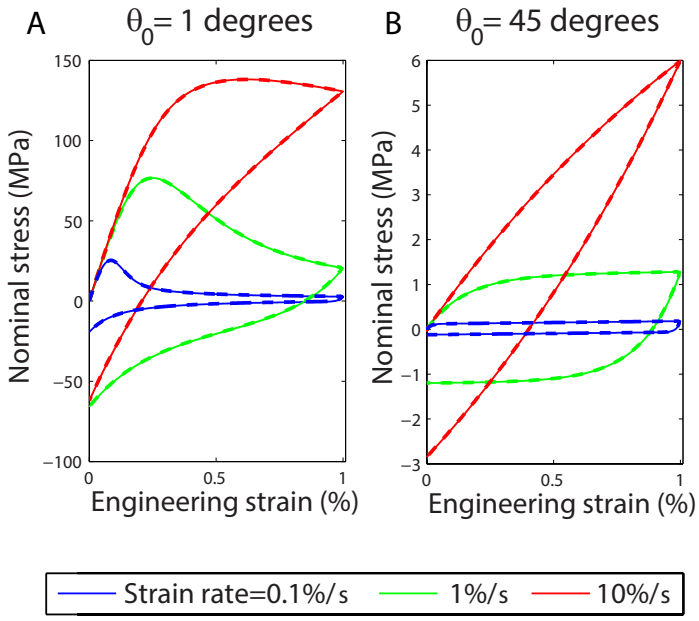

Figure 6: Comparison between the finite deformation theory and finite deformation finite element simulations for viscoelastic composites. The theory is shown in solid line; simulations, shown in dashed lines, are indistinguishable from the theory for different values of the initial angle, θ_0, and a wide range of strain rates.

3.2.2. Loading in the layer direction ($\theta_0 \approx 0$)

The response of composites loaded in the layer direction was simulated using a small initial value for θ_0, in order to take into account the presence of a small imperfection. When the strain amplitude is low (0.2%), the composite behaves like a linear elastic material at high (10%/s) and moderate (1%/s)

strain rates (Fig. 7A). However, at a low strain rate (0.1%/s), the response is highly nonlinear due to buckling (with an infinite wavelength), since the angle θ increases quickly (Fig. 7B) at the same strain amplitude at which the stress deviates from the linear elastic response (at the point depicted by a $*$). For a higher strain amplitude (1%), nonlinearities in the response and buckling are apparent at all strain rates (Figs. 7C and D). Because a (very small) non-zero value is used for the initial angle, there is no true bifurcation, such that the angle increases monotonically during loading. However, the rate of increase of the angle (i.e., the angular velocity) changes dramatically at the strain that corresponds to the departure from a linear response in the stress vs strain curve. The transition from a very low angular velocity to a much higher angular velocity tends to be less visible as the strain rate is increased. In all cases, the initial stress response is characteristic of a linear elastic response. Before buckling, material A carries most of the load; material B is not deformed in shear. However, at finite strains the composite buckles, characterized by a change in the slope of the stress-strain response (depicted by a $*$). The post-buckling slope is negative in these simulations. When the composite buckles, there is a large area within the stress-strain curve, implying large energy dissipation. This energy dissipation is a consequence of the viscoelasticity of material B and of the large shear deformation of material B due to the rotation of the layers in the postbuckling regime.

The buckling strain tends to increase as the strain rate increases in Fig. 7. This dependence of the buckling strain was further investigated in Fig. 8 in which the relationship between the the critical buckling strain and the strain rate is observed to be monotonic. At low strain rate, the curve tends

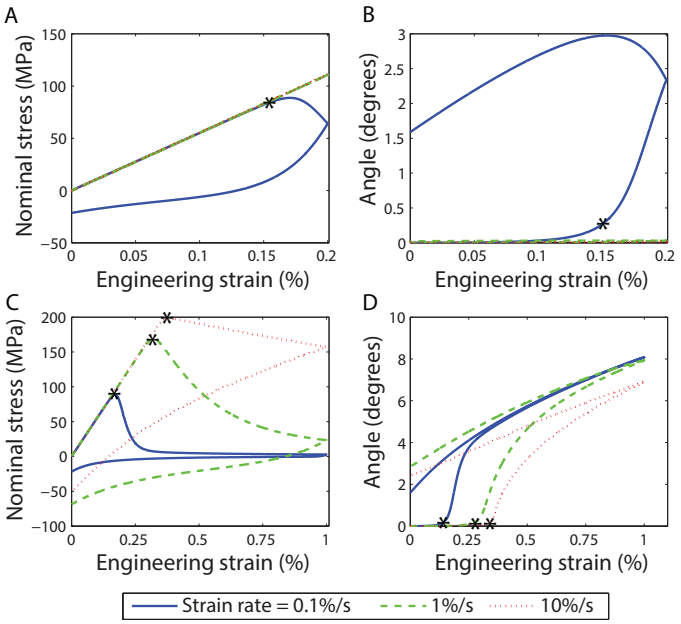

Figure 7: Constant strain rate responses for $.1\%/s$, $1\%/s$ and $10\%/s$ at low and high compressive strains. A. Stress vs. strain, $\epsilon_{max} = 0.2\%$ B. Angle vs. strain, $\epsilon_{max} = 0.2\%$ C. Stress vs. strain, $\epsilon_{max} = 1\%$ D. Angle vs. strain, $\epsilon_{max} = 1\%$. The critical buckling points are identified by $*$.

to converge to the value obtained using a linear buckling analysis when $E_B = E_B^{(\infty)}$, the long term Young's modulus for material B; at high strain rate, the curve tends to converge to the value obtained using a linear buckling analysis when $E_B = E_B^{(0)}$, the short term Young's modulus for material B. Note that a small difference can be observed between the value at a large strain rate and the linear buckling critical strain for $E_B = E_B^{(0)}$. This difference might be due to the fact that the buckling analysis is a linear theory that neglects nonlinear effects.

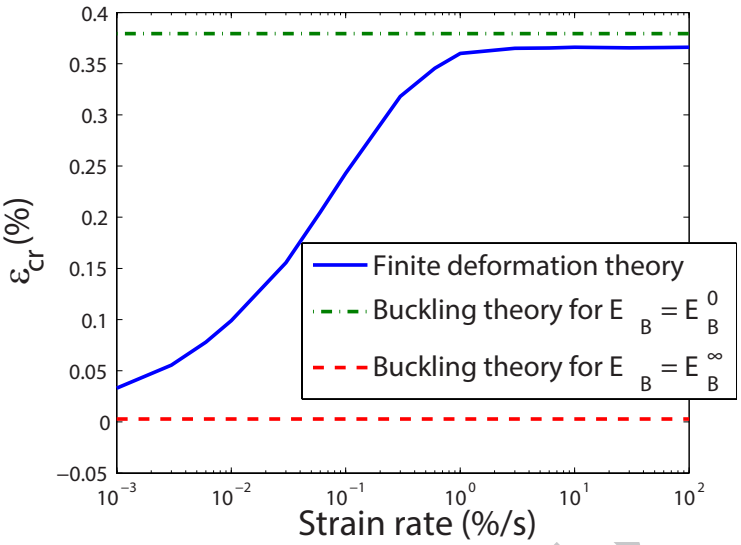

Figure 8: Critical buckling strain vs strain rate obtained using the viscoelastic finite deformation theory. The dashed line and the dashed-dotted lines correspond to the critical strains obtained using a linear buckling analysis for $E_B = E_B^{(\infty)}$ and $E_B = E_B^{(0)}$, respectively.

3.2.3. Response of hyperelastic layered composites

Buckling is also visible in the constant strain rate response of elastic layered composite for $\theta_0 \approx 0$ (Figs. 9A and B). The strain energy of material A (computed using Eq. 28) increases at a fast rate prior to buckling for $\theta_0 \approx 0$. For higher values of θ_0, buckling is not apparent and the strain energy of material A increases monotonically at a much lower rate (see for example $\theta_0 = 45$ degrees). As discussed in [31], for high values of the initial angle, the composite does not buckle, but the layers rotate upon loading (hence the strain energy of material A remains very small because A is not deformed). While the slope of the stress vs strain curve is negative in the

post-buckling regime in the case of viscoelastic layered composites (Fig. 7), the slope of the stress vs strain remains positive in the post-buckling regime if the constituents are not viscoelastic (Figs. 9A and B).

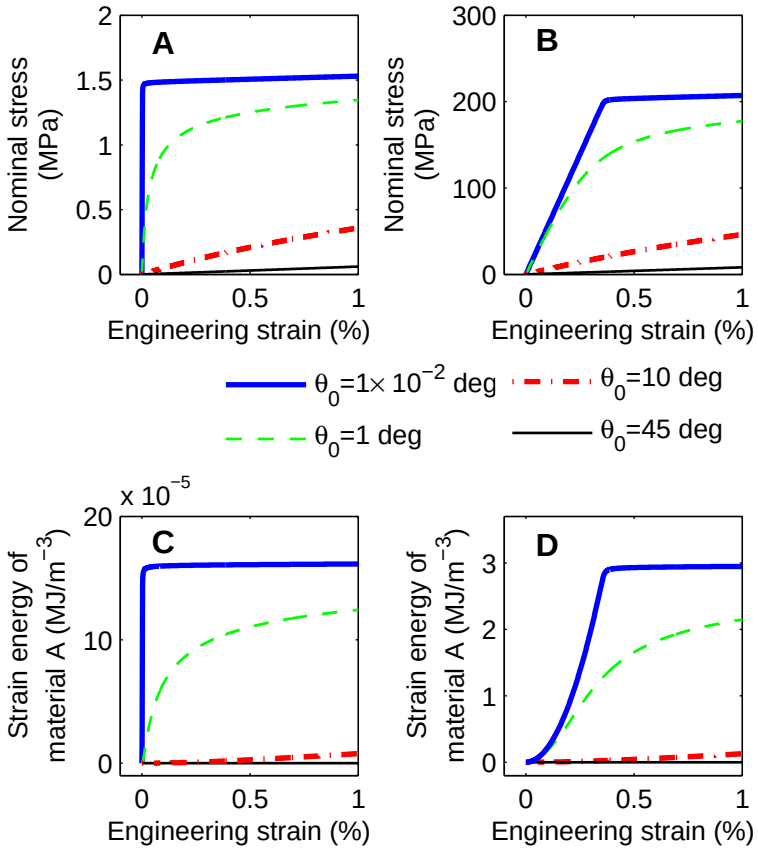

Figure 9: Finite deformation mechanics of hyperelastic layered composites for A and C. $E_B = E_B^{(\infty)}$, the long-term Young's modulus, and B and D. $E_B = E_B^{(0)}$, the short term Young's modulus. In A and B, the macroscopic stress is plotted as a function of macroscopic strain. In C and D, the strain energy (per unit volume) of material A is plotted as a function of the macroscopic strain.

3.2.4. Effect of the initial angle

The influence of the initial angle, θ_0, on the constant strain rate response is analyzed in Fig. 10. When the initial angle is small ($\theta_0 = .1°$), the initial response is linear elastic, since the slope of the response is constant and does not depend on the strain rate. As strain increases, there is an abrupt change in the slope of the response (depicted by a $*$). Beyond this critical point, the slope of the response is negative. The value of the strain at the critical point, and the slope of the response after this critical point, depends strongly on the strain rate. As the initial angle is increased, the initial linear elastic response and the critical point become less and less visible. Furthermore, for $\theta_0 = 10°$ and $\theta_0 = 45°$, the slope of the response is never negative. Additionally, we also note that at higher angles, the nominal stresses in the composite are lower. For the large initial angles, the response is characteristic of a linear viscoelastic material. True buckling is a bifurcation that occurs in the limit $\theta_0 \to 0$. As the size of the imperfection (parametrized by θ_0) is increased, a more progressive transition from the pre-buckling to the post-buckling regime is observed.

3.2.5. Effect of compressibility

The finite deformation theory that was derived assumes that the two constituents are incompressible. While this assumption is a good approximation for polymers and rubber-like materials, it does not hold for materials like steel. Fig. 11 compares the stress vs. strain response for two different values for the Poisson's ratio of material A ($\nu_A = 0.3$ and $\nu_A = 0.5$). The Young's modulus in this instance is such that the plane strain modulus is the same (*i.e* $\frac{E_A}{1-\nu^2}$ is a constant). Barely any difference can be discerned

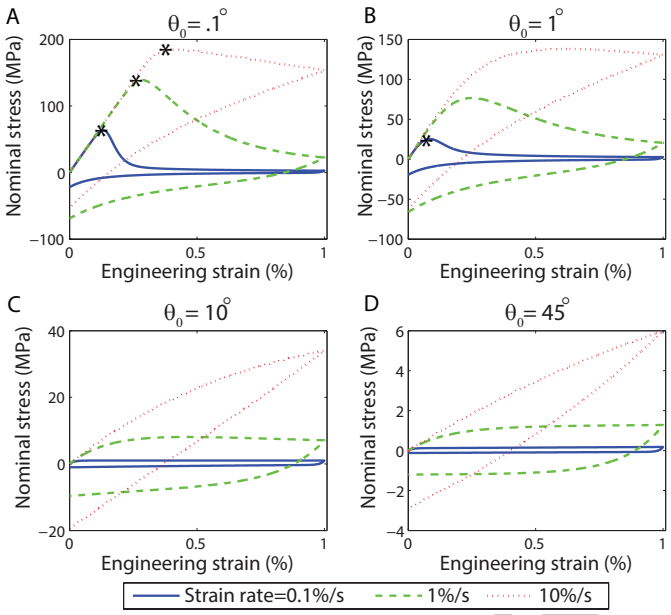

Figure 10: Constant strain rate responses for $.1\%/s$, $1\%/s$ and $10\%/s$ at various initial angles. A. Stress vs. strain, $\theta = .1°$ B. Stress vs. strain, $\theta = 1°$ C. Stress vs. strain, $\theta = 10°$ D. Stress vs. strain, $\theta = 45°$

between the two responses which indicates that assuming incompressibility does not affect the numerical results as long as the change in the effective plane strain stiffness is accounted for accordingly. This near independence of the numerical results on the Poisson's ratio is likely due to the fact that the deformation of material A is nearly isochoric in the postbuckling regime even if A is compressible.

3.2.6. Effect of a finite height

While numerical results for composites of infinite size are interesting, any manufactured composite would have a finite size. Furthermore, for mechanical testing of such a composite, the horizontal displacement on the top and

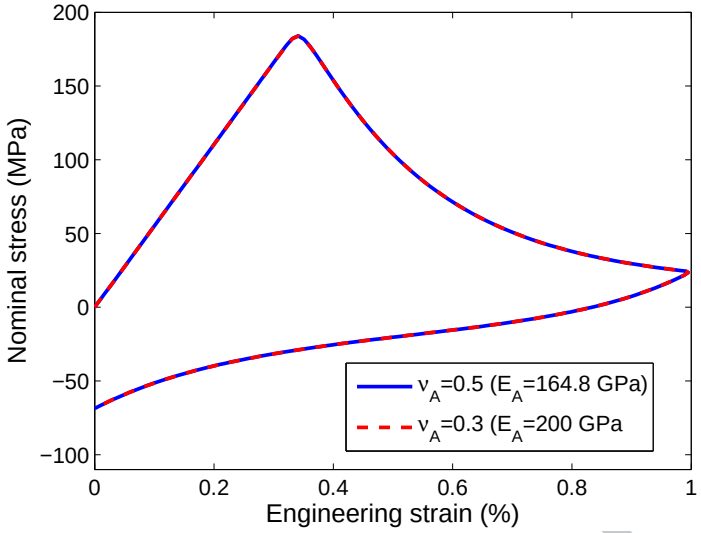

Figure 11: Stress vs. strain response for the incompressible ($\nu_A = 0.5$) and compressible cases ($\nu_A = 0.3$). The results are for $\theta_0 = 1 \times 10^{-2} deg$ and $\dot{\epsilon} = 1\%/s$. For the compressive case, the results were obtained using finite element simulations.

bottom boundaries might have to be fixed. The effect of a finite height was investigated using the following boundary conditions:

$$\begin{aligned} U_Z|_{top} &= U_Z|_{bottom} = 0 \\ U_X|_{top} &= U(t) \\ U_X|_{bottom} &= 0 \end{aligned} \tag{30}$$

where the X and Z directions are represented in Fig. 1, $U(t)$ is the prescribed displacement on the top boundary. Periodic boundary conditions were used for the left and right boundaries using Eqs. 24 and 25 (*i.e.*, we assumed that the number of layers is infinite). Buckling analysis and finite deformation simulations show that the height of the composite can have a dramatic effect on the finite deformation response. Fig. 12A depicts the critical buckling

strain as a function of the height for the upper and lower bounds of E_B. In both cases, as the height of the model is increased, the critical buckling strain converges to the theoretical value for a model of infinite height. While the buckling wavelength is infinite in the case of the composite of infinite size, the buckling wavelength, L_{cr}, is equal to the height of the model in the case of a finite height with these boundary condititions (Fig. 12C). In the non-dilute case (also called longwave mode by Li *et al.* [19]), buckling is a macroscopic instability that is affected by the boundary conditions [8, 21]. Fig. 12B is the stress vs strain response attained through finite deformation simulations. Once again, as the height of the model is increased, the response converges towards the response for the composite of infinite height. Note that both for the critical strain and the stress vs strain curve there is a small difference between the results obtained the theoretical finite deformation model and the numerical simulations with a large size: the critical strain and the stress are slightly higher in the finite height case than in the theoretical model for infinite height. This small difference is due to the fixed horizontal displacement on the top and bottom boundaries in the finite height simulations, which tends to constrain the mode of deformation (the applied boundary conditions correspond to an incompressible deformation). However, despite these small differences, these numerical results demonstrate that the finite deformation model for composites of infinite height can capture very well the stress vs strain response for composites of finite height, provided that $H/W \gtrsim 50$.

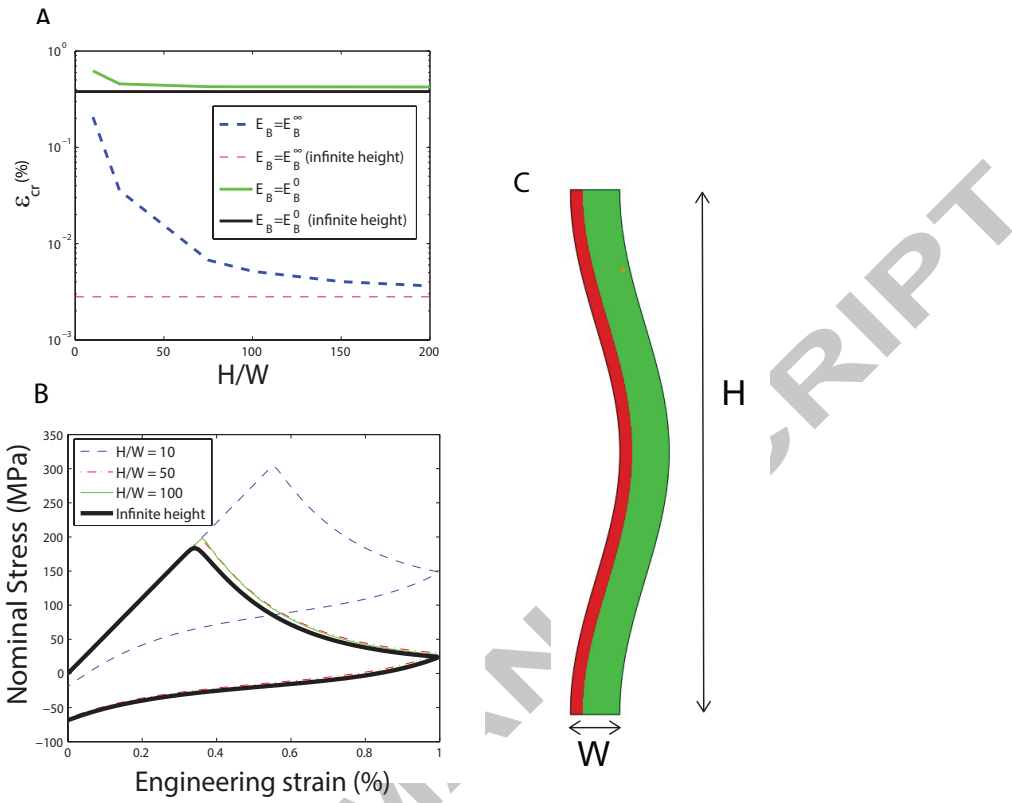

Figure 12: A. Critical buckling strain vs height for $E_B = E_B^\infty$ and $E_B = E_B^0$. B. Stress vs strain response for various heights compared to that of infinite height. The numerical results are for $\theta_0 = 1 \times 10^{-2} deg$ and $\dot{\epsilon} = 1\%/s$

. C. Buckled shape of a unit cell of width W for a composite of finite height, H, and infinite number of layers.

3.3. Effect of prestrain on dynamic properties under cyclic loading

Because of the dramatic effect of buckling on the stress vs strain curve of these viscoelastic layered composites, the effect of prestrain on their dynamical mechanical properties was investigated. The dynamical mechanical properties, typically measured using DMA (with or without prestrain) are

mechanical properties that characterize the response of a material to cyclic loading [18]. For these numerical results, the strain is given by the equation:

$$\begin{aligned} \varepsilon(t) &= \dot{\varepsilon} t \text{ if } 0 < t < t_r \\ &= \varepsilon_0 \text{ if } t_r < t < t_s \\ &= \varepsilon_0 + \Delta\epsilon \sin(2\pi f t) \text{ if } t > t_s \end{aligned} \tag{31}$$

where t_r is the rise time, t_s is the time of the start of the harmonic loading, $\dot{\epsilon}$ is the strain rate ($\dot{\epsilon} = \epsilon_0/t_r$), ϵ_0 is the prestrain, f is the frequency of the cyclic loading and $\Delta\epsilon$ is the amplitude of the cyclic loading. $\epsilon(t)$ is represented graphically in Figs. 13A and 13B. In all the cases considered in this section, $\Delta\varepsilon$ is $1 \times 10^{-3}\%$, $f = 1$ Hz while ε_0 is varied. The numerical results at different frequencies would be qualitatively similar. The stress response for one particular case is shown in Figs. 13C and 13D. In this case, the nominal stress increases until the prestrain value is reached because the prestrain is below the critical strain. Then, as the strain is held constant, the stress gradually decreases and reaches a steady state value close to the initial value (due to viscoelastic stress relaxation). Harmonic loading results in a hysteresis loop. The dynamic Young's modulus, $|E^*|$, (which is a measure of stiffness under cyclic loading), and the loss factor, η (which is a measure of damping) were computed for the last cycle (Fig. 13D) of harmonic loading using the equations given in Appendix A.

Since the buckling shape (Fig. 5C) of a non-dilute composite with initially vertical layers ($\theta_0 \approx 0$) is similar to the undeformed shape of a layered composite with $\theta_0 \neq 0$, we compared the finite deformation simulation of the cyclic loading with a prestrain for $\theta_0 \approx 0$ to the linear viscoelastic theory (without prestrain) of composites with $\theta_0 \neq 0$. We first computed the value

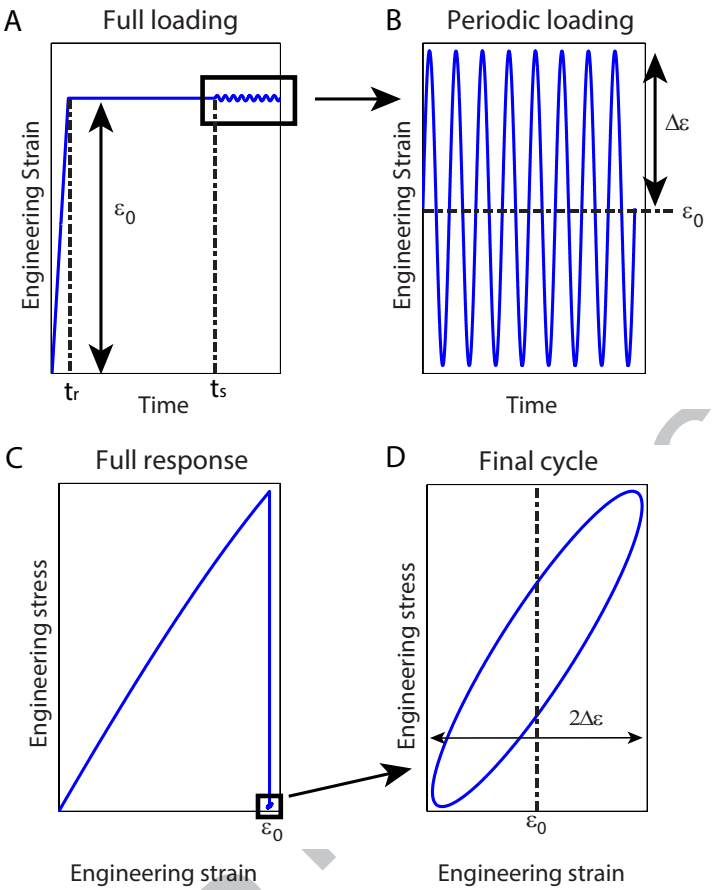

Figure 13: Engineering strain vs time for A. The entire loading cycle. B. The harmonic loading. And the stress vs strain response for C. The entire loading cycle. D. The final cycle.

of the angle $\theta_s(\epsilon_0)$, that is reached after prestraining the composite with initially vertical layers to a prestrain of value ϵ_0, which is held constant until the stress relaxes to a constant value (see Fig. 14A). We then computed $|E^*|$ and η using the linear viscoelastic theory for $\theta_0 = \theta_s(\epsilon_0)$ (Fig. 14B) by adapting the equations given in [23] to the plane strain case (see Appendix B).

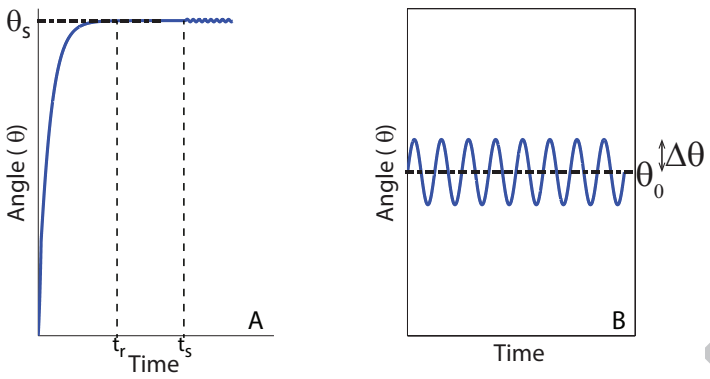

Figure 14: Angle, θ, vs time for A. Harmonic loading after prestrain. After holding the strain at the prestrain value, θ converges to a constant value, θ_s. B. Harmonic loading without prestrain with an initial angle, θ_0. The amplitude of the oscillations in the angle is $\Delta\theta$

Figs. 15A and B show the stiffness and damping values as functions of prestrain. As the prestrain is increased from 0 to 10%, the effective dynamic modulus decreases by two orders of magnitude (for ϕ_A=25%) and the damping increases by two orders of magnitude. These results are due to the rotation of the layers as the prestrain is increased. On the same graphs, the value obtained using the linear viscoelastic theory using an initial angle, $\theta_0 = \theta_s(\epsilon_0)$, are plotted as a function of ϵ_0. There is an agreement in the general trend between the finite deformation theory with prestrain and linear viscoelastic theory with an initial angle. Some small differences are visible at the highest prestrain values. These differences are likely due to the fact that the geometry of buckling mode shape is not exactly identical to the geometry of undeformed composites with $\theta \neq 0$ (see Fig. 5C). Furthermore, after prestraining the composite, the non-zero stress values in the two constituents might affect the response of the composite to the cyclic load.

The dynamic modulus is plotted as a function of the damping in the stiffness-loss map shown in Fig. 15C. Each point of each line corresponds to the values obtained for $|E^*|$ and η at a fixed prestrain value. As the prestrain is increased the points first move toward the right side of the figure (indicating a large increase in the damping and small reduction in the stiffness), before moving towards the bottom (indicating a large decrease in the stiffness and a small increase in the damping). The same effect is obtained by simulating composites with increasing angle (in the small strain regime).

4. Discussion and conclusions

4.1. Analytical and numerical investigation of the nonlinear mechanics of viscoelastic composites

In this paper, we investigated the nonlinear mechanics of viscoelastic layered composites. Due to the remarkable simplicity of the microstructure and mode of deformation, analytical expressions could be derived for the finite deformation of non-dilute composites. Theoretical results were shown to match results from finite element simulations. Elastic buckling analysis helped to determine the source of the nonlinear nature of the stress vs strain response. Geometric softening due to buckling is responsible for the strong nonlinearity in the stress vs strain curve, which explains the nonlinearity in the stiffness and damping that was previously observed in finite deformation finite element simulations [23]. In the postbuckling regime, the layers tend to rotate upon loading, which reduces the effective stiffness of the composites. Due to this geometric softening (due to the rotation of the layers) and to the time-dependent decrease in the effective stiffness of the viscoelastic

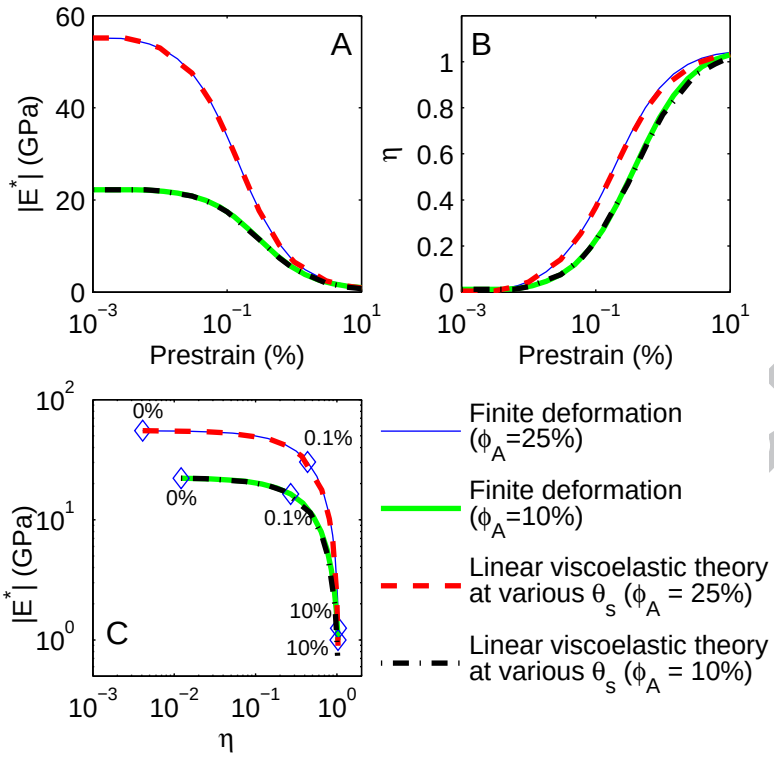

Figure 15: Comparison between the finite deformation theory and the linear viscoelastic theory for a composite with an initial angle $\theta_0 = \theta_s$. A. Dynamic modulus vs. prestrain. B. Damping vs. prestrain. C. Stiffness loss map for various volume fractions (points along each line are for varying ϵ_0). Values obtained for ϵ_0 =0, 0.1 and 10% are depicted by diamond symbols.

constituent, a negative slope is observed in the constant strain rate response of viscoelastic layered composites.

While the focus of this paper was on the mechanics of layered composites, parts of the results might be qualitatively similar for other types of composite microstructures. The rate-dependent buckling and negative slope in the post-buckling regime that were observed here are caused by the presence of a time-

dependent Young's modulus for the soft material (*i.e.*, viscoelasticity) and of geometric softening. More complex microstructures, that exhibit strong geometrical nonlinearities, would have similar characteristics. Furthermore, while neo-Hookean constitutive models were used here for the derivation of the theoretical model, using other types of constitutive models would lead to similar finite deformation responses (see for example the numerical results shown in [23]).

4.2. The stiffness and damping of viscoelastic layered composites can be tuned by prestrain

Our findings might be used to design layered composites with simultaneously high stiffness and high damping. In a previous paper, Meaud *et al.* [23] demonstrated that excellent dynamic properties can be achieved by selecting optimal values for the angle between the layer direction and the load direction. We have shown in this paper that almost identical properties are obtained by applying a small amount of prestrain to layered composites with layers that are in the load direction prior to the application of the prestrain. There is a well known tradeoff between stiffness and damping in common engineering and natural materials [18]. Simultaneously optimizing stiffness and damping for a category of composite materials is a multiobjective optimization problem with competing objectives, for which a Pareto set of optimal designs can be defined [23]. For layered composites with a given volume fraction and given constitutive materials, the amount of prestrain allows one to move along the Pareto set and to tune by orders of magnitude the values of the stiffness and damping in response to cyclic loads of small amplitudes. This dramatic change in the mechanical properties is reversible since it is a

consequence of the buckling instability and to the rotation of the layers.

Composites with initially vertical layers also have interesting properties in response to loads of finite amplitude. Without any prestrain, the composites have an excellent load-bearing capacity due to their high stiffness. In the event of a load of large amplitude, the structures will buckle, thus allowing the viscoelastic constituent to dissipate a very large amount of mechanical energy. Furthermore, even though the mode of deformation and the buckling strains are affected by the boundary conditions of layered composites of finite size, the height only needs to be about 50 times the unit cell width to achieve a similar stress vs strain response to a layered composites of infinite size.

4.3. Dilute viscoelastic layered composites

While the finite deformation of viscoelastic dilute layered composites was not addressed in this paper, it might be a promising area of future research. Due to their wavy mode of deformation, the case of dilute elastic layered composites, previously investigated by Li *et al.* [19], can be used to create bandgaps for elastic wave propagation [31]. For dilute layered composites with viscoelastic constituents, the elastic buckling analysis suggests that the mode of deformation should be rate-dependent and time-dependent: the buckling shape might switch from an infinite wavelength to a finite wavelength depending on the volume fraction and strain rate. This interesting behavior might be used to design adaptive materials with tunable and multifunctional properties. More generally, viscoelasticity and rate dependence might be exploited to expand the design-space for materials with unconventional mechanical properties or multifunctional characteristics.

Acknowledgments: This research was supported by startup funds from the Georgia Institute of Technology. The authors thank Thomas Bowling for proof-reading the manuscript.

Appendix A. Computation of the dynamic modulus and loss factor

In order to determine the effective stiffness and damping of layered composites with prestrain, we used the approach described here that can directly be applied even in the case of a nonlinear response. The values obtained with the proposed definitions match the conventional definitions for linear viscoelastic materials at infinitesimal strains without prestrain. In the case of a linear viscoelastic material, after reaching steady-state during the cyclic part of Eq. 31, the stress can be written as:

$$\sigma(t) = \Delta\sigma \sin(\omega t + \delta) + \sigma_0 \tag{A.1}$$

where $\Delta\sigma$ is the amplitude of the stress curve, δ corresponds to the phase lag and ω is the radian frequency of the excitation. σ_0 is the static stress value which occurs when the strain is equal to ε_0.

In this paper we consider the effective stiffness of a layered viscoelastic composite as the absolute value of its dynamic modulus, $|E^*|$, which can be obtained graphically by analyzing the stress versus strain response of the composite. The overall effective stiffness is obtained by dividing the difference between the maximum and minimum values of the stress, $\sigma_{max} - \sigma_{min} = 2\Delta\sigma$, by the difference between the maximum and minimum value of the strain, $\epsilon_{max} - \epsilon_{min} = 2\Delta\epsilon$. $|E^*|$ corresponds to the slope of the line that connects the lower left corner to the upper right corner of the box as shown in Fig A.16A for a linear viscoelastic material. We propose to extend this graphical interpretation to define the effective stiffness of a nonlinear viscoelastic material, as shown in A.16B.

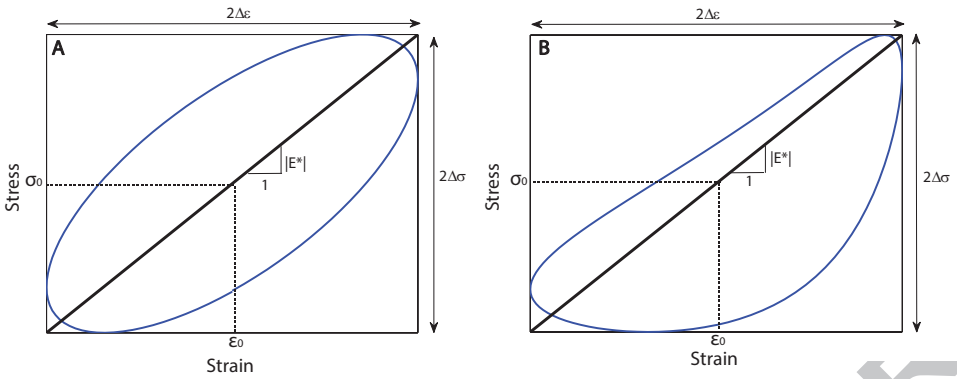

Figure A.16: Force displacement boundary along with line depicting the dynamic modulus, $|E^*|$. A. Shown for a linear viscoelastic material. B. Shown for a nonlinear viscoelastic material

In the case of a linear viscoelastic material, damping is commonly defined as the tangent of the phase lag, $\tan(\delta)$, between stress and strain. However, when nonlinearities affect the response of the material at finite strain amplitudes, the damping cannot be evaluated using $\tan(\delta)$ since the stress is no longer a harmonic function of time. A more general definition of damping is needed. This can be obtained by noting the link between $\tan(\delta)$ and energy dissipation in the case of a linear viscoelastic material. The energy dissipated per cycle per unit volume, W_d, can be computed using the following equation:

$$W_d = \int_0^T \sigma(t) \frac{d\varepsilon}{dt}\, dt \tag{A.2}$$

Where $T = 2\pi/\omega$ is the period of the input. Computing the integral in Eq. A.2 we get:

$$W_d = \pi \Delta\varepsilon \Delta\sigma \sin(\delta) \tag{A.3}$$

Solving Eq. A.3 for $tan(\delta)$ we get

$$tan(\delta) = \tan\left[\sin^{-1}\left(\frac{W_d}{\pi\Delta\varepsilon\Delta\sigma}\right)\right] \tag{A.4}$$

We note that $\pi\Delta\varepsilon\Delta\sigma$ corresponds to the maximum energy per cycle that a linear viscoelastic material can dissipate for given values of $\Delta\varepsilon$ and $\Delta\sigma$. Let $W_d^{max}(\Delta\varepsilon, \Delta\sigma)$ be this value. We can then write for a linear viscoelastic material:

$$\tan(\delta) = \tan\left[\sin^{-1}\left(\frac{W_d}{W_d^{max}(\Delta\varepsilon, \Delta\sigma)}\right)\right] \tag{A.5}$$

We propose in this paper to define the effective loss factor for a nonlinear viscoelastic material, η, to be:

$$\eta = \tan\left[\sin^{-1}\left(\frac{W_d}{W_d^{max}(\Delta\varepsilon, \Delta\sigma)}\right)\right] \tag{A.6}$$

Graphically, W_d corresponds to the area with the stress-strain curve and $W_d^{max}(\Delta\varepsilon, \Delta\sigma)$ corresponds to the ellipse whose area is $\pi\Delta\epsilon\Delta\sigma$. This is graphically shown in Figs. A.17A and A.17B.

Appendix B. Plane strain linear viscoelastic theory

Meaud and Hulbert [23] derived the complex Young's moduli for Reuss composites (loading in the z direction, see Fig. 1) and Voigt composites (loading in the x direction) in response to dynamic loading for the generalized plane strain case (*i.e*, the out of plane dimension is assumed infinite such that the normal strains in the two phases are identical in the out of plane direction). These equations are adapted here to the plane strain case.

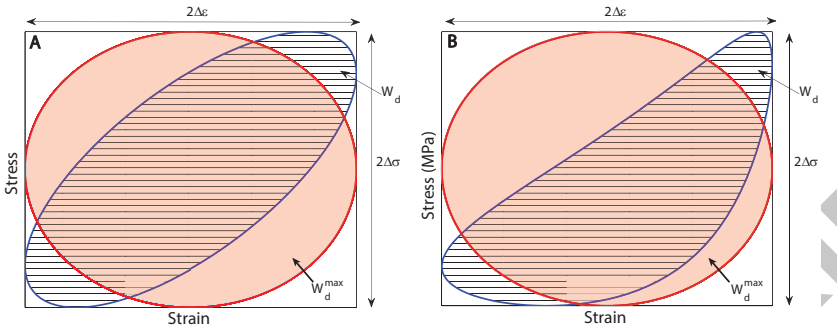

Figure A.17: Energy dissipated along with maximum energy dissipated within the same stress-strain boundary. A. Linear viscoelastic material. B. Nonlinear viscoelastic material.

Applying the condition $\epsilon_y^A = \epsilon_y^B = 0$ to constitutive equations 10 and 13 from Liu *et al.* [20] in conjunction with equilibrium equations 15 through 17 and kinematic equations 18 through 20 we derive the Young's modulus for the Reuss configuration, E_z^{eff}.

$$E_z^{eff} = \frac{E_A E_B}{\phi_A E_B + \phi_B\big(E_A(1-\nu_B^2) + E_B\nu_A(1+\nu_B)\big) + \frac{q_1\phi_B\nu_B\left(\nu_A E_B - E_A(1+\nu_B)\right)}{q_2}} \tag{B.1}$$

where q_1 and q_2 are:

$$q_1 = E_B\nu_A\phi_A(\nu_A+1) - E_A\nu_B\phi_A(\nu_B+1) \tag{B.2}$$

$$q_2 = E_B\phi_B(\nu_A^2-1) + E_A\phi_A(\nu_B^2-1) \tag{B.3}$$

For the Voigt configuration we use the same constitutive equations but use equilibrium equations 23 through 25 and kinematic equations 26 through

28 from Liu *et al.* [20] to solve for E_x^{eff}.

$$E_x^{eff} = \frac{\phi_A E_A}{1-\nu_A^2} + \frac{\phi_B E_B}{1-\nu_B^2} \tag{B.4}$$

The effective modulus in the X direction is then computed using Eq. 15 given in [23].

Appendix C. Finite deformation viscoelastic model in ABAQUS

According to [10], the deviatoric part of the Kirchoff stress, $\boldsymbol{\tau}^D(t)$, is given by the following expression for finite deformation viscoelastic models in ABAQUS:

$$\boldsymbol{\tau}^D(t) = \boldsymbol{\tau}_0{}^D(t) + dev\Big[\int_0^t \frac{\dot{G}(\tau')}{G_0}\bar{\mathbf{F}}_{\mathbf{t}}^{-\mathbf{1}}(t-\tau')\boldsymbol{\tau}_0^D(t-\tau')\bar{\mathbf{F}}_{\mathbf{t}}^{-\mathbf{T}}(t-\tau')d\tau'\Big] \tag{C.1}$$

where $\boldsymbol{\tau}_0{}^D(t)$ is the instantaneous deviatoric part of the Kirchoff stress, G_0 is the instantaneous shear modulus and $\bar{\cdot}$ denotes the isochoric part. Since the material is assumed to be incompressible,

$$\boldsymbol{\tau}^D(t) = J\boldsymbol{\sigma}^D(t) = \boldsymbol{\sigma}^D(t) \text{ and } \bar{\mathbf{F}}_{\mathbf{t}}^{-\mathbf{T}}(t-\tau') = \mathbf{F}_{\mathbf{t}}^{-\mathbf{T}}(t-\tau') \tag{C.2}$$

$\mathbf{F_t}(t-\tau')$ is given by:

$$\mathbf{F}(t-\tau') = \mathbf{F_t}(t-\tau')\mathbf{F}(t) \tag{C.3}$$

Therefore

$$\bar{\mathbf{F}}_{\mathbf{t}}^{-\mathbf{1}}(t-\tau') = \mathbf{F}^{-\mathbf{1}}(t)\mathbf{F}^{-\mathbf{1}}(t-\tau') \text{ and } \bar{\mathbf{F}}_{\mathbf{t}}^{-\mathbf{T}}(t-\tau') = \mathbf{F}^{-\mathbf{T}}(t-\tau')\mathbf{F}^{-\mathbf{T}}(t) \tag{C.4}$$

Therefore the deviatoric part of the Cauchy stress is given by:

$$\boldsymbol{\sigma}^D(t) = \boldsymbol{\sigma}_0^D(t) + dev\Big[\mathbf{F^{-1}}(t)\int_0^t \frac{\dot{G}(\tau')}{G_0}\mathbf{F^{-1}}(t-\tau')\boldsymbol{\sigma}_0^D(t-\tau')\mathbf{F^{-T}}(t-\tau')d\tau'\mathbf{F^{-T}}(t)\Big] \tag{C.5}$$

Using the change of variable $\tau = t - \tau'$, this equation can be written:

$$\boldsymbol{\sigma}^D(t) = \boldsymbol{\sigma}_0^D(t) + dev\Big[\mathbf{F^{-1}}(t)\int_0^t \frac{\dot{G}(t-\tau)}{G_0}\mathbf{F^{-1}}(\tau)\boldsymbol{\sigma}_0^D(\tau)\mathbf{F^{-T}}(\tau)d\tau\mathbf{F^{-T}}(t)\Big] \tag{C.6}$$

Since the deviatoric part of the instantaneous 2nd Piola Kirchoff stress, $\mathbf{S_0^D}(\tau)$, is given by:

$$\mathbf{S_0^D}(\tau) = \mathbf{F^{-1}}(\tau)\boldsymbol{\sigma}_0^D(\tau)\mathbf{F^{-T}}(\tau), \tag{C.7}$$

the equation for $\boldsymbol{\sigma}^D(t)$ can be written:

$$\boldsymbol{\sigma}^D(t) = \boldsymbol{\sigma}_0^D(t) + dev\Big[\mathbf{F^{-1}}(t)\int_0^t \frac{\dot{G}(t-\tau)}{G_0}\mathbf{S_0^D}(\tau)d\tau\mathbf{F^{-T}}(t)\Big] \tag{C.8}$$

After integration by part, we obtain:

$$\boldsymbol{\sigma}^D(t) = dev\Big[\mathbf{F^{-1}}(t)\int_0^t \frac{G(t-\tau)}{G_0}\dot{\mathbf{S_0^D}}(\tau)d\tau\mathbf{F^{-T}}(t)\Big] \tag{C.9}$$

For a 1 term Prony series, the relaxation modulus is given by:

$$G(t) = \Big[1 + \beta_\alpha^\infty exp(-\frac{t}{\tau_\alpha})\Big]G_\infty \tag{C.10}$$

where G_∞ is the long term shear modulus, τ_α is the relaxation time constant and $\Big[1 + \beta_\alpha^\infty\Big]G_\infty = G_0$ is the instantaneous shear modulus. $\boldsymbol{\sigma}^D(t)$ can be written:

$$\boldsymbol{\sigma}^D(t) = \boldsymbol{\sigma}_\infty^D(t) + dev\Big[\mathbf{F^{-1}}(t)\mathbf{Q}_\alpha(t)\mathbf{F^{-T}}(t)\Big] \tag{C.11}$$

where $\boldsymbol{\sigma}^D_\infty(t)$ is the long-term deviatoric Cauchy stress and $\mathbf{Q}_\alpha(t)$ is given by:

$$\mathbf{Q}_\alpha(t) = \int_0^t \beta^\infty_\alpha exp(\frac{-(t-\tau)}{\tau_\alpha})\dot{\mathbf{S}^{\mathbf{D}}_{\mathbf{0}}}(\tau)d\tau \tag{C.12}$$

It is easy to prove that $\mathbf{Q}_\alpha(t)$ is solution to Eq. 13. The deviatoric part of the 2nd Piola-Kirchoff stress can be written:

$$\boldsymbol{S}_D(t) = \mathbf{S}^{\mathbf{D}}_\infty(t) + \mathbf{Q}_\alpha(t) \tag{C.13}$$

where $\boldsymbol{S}_D(t) = \mathbf{F^{-1}}(t)\boldsymbol{\sigma}^D(t)\mathbf{F^{-T}}(t)$ is the deviatoric part of the 2nd Piola-Kirchoff stress and $\boldsymbol{S}^D_\infty(t) = \mathbf{F^{-1}}(t)\boldsymbol{\sigma}^D_\infty(t)\mathbf{F^{-T}}(t)$ is the long term part of the deviatoric part of the 2nd Piola-Kirchoff stress. Hence, the finite deformation viscoelastic model used in ABAQUS is equivalent to the model used for the theoretical finite deformation algorithm.

References

[1] Ashby, M., 1989. Overview no. 80: On the engineering properties of materials. Acta Metallurgica 37 (5), 1273 – 1293.

[2] Bertoldi, K., Boyce, M., Deschanel, S., Prange, S., Mullin, T., 2008. Mechanics of deformation-triggered pattern transformations and superelastic behavior in periodic elastomeric structures. Journal of the Mechanics and Physics of Solids 56 (8), 2642–2668.

[3] Bhalerao, M., Moon, T., 1996. On the growth-of-waviness in fiber-reinforced polymer composites: viscoelastic bifurcation and imperfection sensitivity. Journal of applied mechanics 63 (2), 460–466.

[4] Biot, M., 1964. Theory of internal buckling of a confined multilayered structure. Geological Society of America Bulletin 75 (6), 563–568.

[5] Biot, M. A., 1964. Mechanics of incremental deformations. Wiley.

[6] Browning, A., Ortiz, C., Boyce, M. C., 2013. Mechanics of composite elasmoid fish scale assemblies and their bioinspired analogues. Journal of the mechanical behavior of biomedical materials 19, 75–86.

[7] Chen, C. P., Lakes, R. S., 1993. Analysis of high-loss viscoelastic composites. Journal of Materials Science 28, 4299–4304.

[8] Geymonat, G., Müller, S., Triantafyllidis, N., 1993. Homogenization of nonlinearly elastic materials, microscopic bifurcation and macroscopic loss of rank-one convexity. Archive for rational mechanics and analysis 122 (3), 231–290.

[9] Hibbit, Karlsson, Sorensen, 2011. ABAQUS/Standard Analysis User's Manual, Version 6.11. Hibbit, Karlsson, Sorensen Inc., USA.

[10] Hibbitt, H., Karlsson, B., Sorensen, P., 2012. Abaqus theory manual, version 6.12. Pawtucket, Rhode Island, USA.

[11] Holzapfel, G. A., 1996. On large strain viscoelasticity: continuum formulation and finite element applications to elastomeric structures. International Journal for Numerical Methods in Engineering 39 (22), 3903–3926.

[12] Holzapfel, G. A., 2000. Nonlinear solid mechanics. Vol. 24. Wiley Chichester.

[13] Huang, R., 2005. Kinetic wrinkling of an elastic film on a viscoelastic substrate. Journal of the Mechanics and Physics of Solids 53 (1), 63–89.

[14] Huang, R., Suo, Z., 2002. Instability of a compressed elastic film on a viscous layer. International Journal of Solids and Structures 39 (7), 1791–1802.

[15] Huang, R., Suo, Z., 2002. Wrinkling of a compressed elastic film on a viscous layer. Journal of Applied Physics 91 (3), 1135–1142.

[16] Im, S., Huang, R., 2005. Evolution of wrinkles in elastic-viscoelastic bilayer thin films. Journal of applied mechanics 72 (6), 955–961.

[17] Keplinger, C., Li, T., Baumgartner, R., Suo, Z., Bauer, S., 2012. Harnessing snap-through instability in soft dielectrics to achieve giant voltage-triggered deformation. Soft Matter 8 (2), 285–288.

[18] Lakes, R., 2009. Viscoelastic materials. Cambridge University Press.

[19] Li, Y., Kaynia, N., Rudykh, S., Boyce, M. C., 2013. Wrinkling of interfacial layers in stratified composites. Advanced Engineering Materials 15 (10), 921–926.

[20] Liu, B., Feng, X., Zhang, S.-M., 2009. The effective young's modulus of composites beyond the voigt estimation due to the poisson effect. Composites Science and Technology 69 (13), 2198–2204.

[21] Lopez-Pamies, O., Ponte Castañeda, P., 2009. Microstructure evolution in hyperelastic laminates and implications for overall behavior and macroscopic stability. Mechanics of Materials 41 (4), 364–374.

[22] Makke, A., Perez, M., Lame, O., Barrat, J.-L., 2012. Nanoscale buckling deformation in layered copolymer materials. Proceedings of the National Academy of Sciences 109 (3), 680–685.

[23] Meaud, J., Hulbert, G., 2013. Dependence of the dynamic properties of voigt and reuss composites on the poisson's ratio and bulk loss factor of the constituent materials. Journal of Composite Materials 47, 3237–3247.

[24] Meaud, J., Sain, T., Hulbert, G. M., Waas, A. M., 2013. Analysis and optimal design of layered composites with high stiffness and high damping. International Journal of Solids and Structures 50 (9), 1342 – 1353.

[25] Mühlhaus, H.-B., Moresi, L., Hobbs, B., Dufour, F., 2002. Large amplitude folding in finely layered viscoelastic rock structures. Pure and Applied Geophysics 159 (10), 2311–2333.

[26] Nestorović, M., Triantafyllidis, N., 2004. Onset of failure in finitely strained layered composites subjected to combined normal and shear loading. Journal of the Mechanics and Physics of Solids 52 (4), 941–974.

[27] Overvelde, J. T., Bertoldi, K., 2014. Relating pore shape to the non-linear response of periodic elastomeric structures. Journal of the Mechanics and Physics of Solids 64, 351–366.

[28] Parnes, R., Chiskis, A., 2002. Buckling of nano-fibre reinforced composites: a re-examination of elastic buckling. Journal of the Mechanics and Physics of Solids 50 (4), 855–879.

[29] Rosen, B., 1965. Mechanics of composite strengthening. Am. Soc. Metals Seminar, Fibre Composite Materials, Metals Park, Ohio, 37–75.

[30] Rudykh, S., Bhattacharya, K., et al., 2012. Snap-through actuation of thick-wall electroactive balloons. International Journal of Non-Linear Mechanics 47 (2), 206–209.

[31] Rudykh, S., Boyce, M. C., 2014. Analysis of elasmoid fish imbricated layered scale-tissue systems and their bio-inspired analogues at finite strains and bending. IMA Journal of Applied Mathematics doi: 10.1093/imamat/hxu005.

[32] Rudykh, S., Boyce, M. C., 2014. Transforming small localized loading into large rotational motion in soft anisotropically structured materials. Advanced Engineering Materials 16 (11), 1311–1317.

[33] Rudykh, S., Boyce, M. C., 2014. Transforming wave propagation in layered media via instability-induced interfacial wrinkling. Physical review letters 112 (3), 034301.

[34] Rudykh, S., deBotton, G., 2012. Instabilities of hyperelastic fiber composites: micromechanical versus numerical analyses. Journal of Elasticity 106 (2), 123–147.

[35] Rudykh, S., Ortiz, C., Boyce, M. C., 2015. Flexibility and protection by design: imbricated hybrid microstructures of bio-inspired armor. Soft matter 11 (13), 2547–2554.

[36] Sain, T., Meaud, J., Yeom, B., Waas, A. M., Arruda, E. M., 2015. Rate dependent finite strain constitutive modeling of polyurethane and polyurethane–clay nanocomposites. International Journal of Solids and Structures 54, 147–155.

[37] Tong, Q., Wang, H., Xu, R., Liu, B., Fang, D., 2014. Adaptive periodical representative volume element for simulating periodical postbuckling behavior. International Journal for Numerical Methods in Engineering 98 (6), 445–468.

[38] Triantafyllidis, N., Maker, B., 1985. On the comparison between microscopic and macroscopic instability mechanisms in a class of fiber-reinforced composites. Journal of applied mechanics 52 (4), 794–800.

[39] Wang, P., Casadei, F., Shan, S., Weaver, J. C., Bertoldi, K., 2014. Harnessing buckling to design tunable locally resonant acoustic metamaterials. Physical review letters 113 (1), 014301.